

Chapter 4 Gradient-Index Axicon

4.1. Introduction

The term axicon was coined in 1954 by John McLeod^{1,2} to describe his newly invented optical element, which produced a line focus. He explored various methods to diffract light so that it converged linearly on the optical axis, but the best-known system was a refractive element with a planar and a conical surface. This element produced an extended focus, which began at the back surface, but McLeod also showed that replacing the planar surface with a spherical surface shifted the initial focus away from the back surface.

Since then, there have been many studies of axicons. Annulus apertures were imaged to create an extended focus.^{3,4} Conical mirror designs— sometimes called reflaxicons—have been studied⁵; these work equivalently to refractive axicons. To produce line foci that began some distance from the back surface, aberrated-lens systems have been investigated. The nominal focus of the lens provided the focal offset, and the spherical aberrations provide the extended focus.⁶ Others have studied the design and performance of diffractive and holographic axicons.⁷

A great variety of gradient-index (GRIN) studies has been concerned with traditional lens design,⁸⁻¹² but there has been little interest in GRIN axicons. Though Marchand¹³ studied the behavior of axicon gradient lenses, he was interested in aberrations of GRIN lenses with odd-power terms in their index polynomials.

González et al.¹⁴ considered the theoretical behavior of a radial-GRIN element with linear index terms (a W-shaped index profile) and showed that it produced ring images, however, they did not explicitly consider the on-axis imaging behavior and made no comment on the focal characteristics.

GRIN axicons provide an alternative to other transmissive axicon designs. One possible use is in optical coherence tomography.¹⁵ For these systems, a long focal region is needed to maximize the image depth. This may, in principle, be provided by an axicon. In other cases, GRIN axicons may have unique qualities that make them a better solution. Although the dispersion of this element is not known, it is reasonable to conclude from studies of other GRIN materials¹⁶ that they would have 2 orders of magnitude less dispersion than diffractive axicons. As indicated by the measurements, the length of a GRIN axicon element affects the performance. Thus, fabrication errors in the index profile can be partially corrected by appropriate length selection. Because several GRIN axicons can be produced from a single ion-diffused glass rod, many axicons can be fabricated by simultaneously diffusing multiple rods. This may provide a more cost-effective solution than custom fabrication of multiple conical elements, lithographic production of a diffractive element, or creation of a master diffractive element for stamping reproduction. In addition, since diffusion works best with small-diameter glass rods, GRIN axicons are well suited for small-aperture systems. Finally, they do not require the alignment necessary with multiple lens solutions.

In this chapter, the design, fabrication, and testing of the first GRIN axicon are described.¹⁷ The index profile is determined by a thin-lens optical path-length (OPL)

argument. Two samples are fabricated by the time-varying boundary conditions (TVBC) method and are examined. They are shown to have an extended focus and to produce a pseudo-Bessel beam, as expected by analogy to an aberrated-lens axicon system.¹⁸

4.2. Thin-Lens Design of a Gradient-Index Axicon

The first step in the design of a GRIN axicon was to determine the index of refraction necessary for a radial-gradient lens to produce an extended focus, with an infinite object distance. The design constrained the line focus to be offset from the back surface.

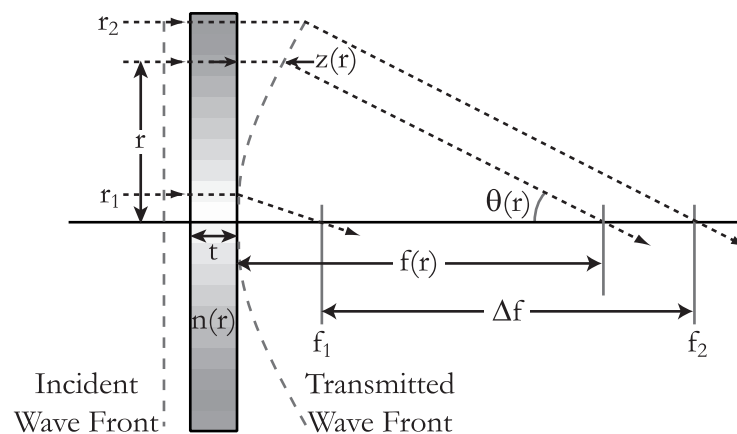


Figure 4.1. Parameters used for deriving the index profile of a GRIN axicon. Note that radial position, r , is always positive, measured from the optical axis.

The necessary index profile was derived with geometrical optics and an optical path-length (OPL) argument, as described in Chapter 3. As seen in Figure 4.1, the axicon is a GRIN lens with planar surfaces, whose back focal length is proportional to incident ray height. The incident light is assumed to be collimated and collinear with

the optical axis. For a first design, a simple focal behavior is desired, and the back focal length is chosen to be

$$f(r) = f_1 + \frac{r - r_1}{r_2 - r_1} \Delta f \text{ where } r \geq 0, \quad (4.1)$$

where r is the radial ray position at the front surface and is always positive ($r \geq 0$), $r_{1,2}$ is the minimum and the maximum incident ray height allowed, $f_{1,2}$ is the back focal length for a ray entering at the ray height $r_{1,2}$, Δf is $f_2 - f_1$ and is equal to the focal region length, and $n(r)$ is the refractive index, as a function of radius.

Assuming a thin sample (or, equivalently, a weak gradient), the index variation experienced by any ray is small, and there is negligible beam displacement in the material. The radial ray position at the emerging wave front is then considered equal to the input position. The wave front displacement $z(r)$ from the back surface describes the emergent wave front. The slope of the wave-front normal is then given by $-dz/dr$. Because the geometrical ray angle is equal to slope of the wave front normal, the wave front is described by the ray angle $\theta(r)$ by

$$\tan(\theta) = -\frac{dz}{dr} \approx -\frac{r}{f(r)}, \text{ where } z(r) \ll f(r), \quad (4.2)$$

where the wave front offset from the back surface is assumed to be much smaller than the back focal distance. With the focal-length expression and the identity

$$\int \frac{x}{a + bx} dx = \frac{x}{b} - \frac{a}{b^2} \ln(a + bx), \quad (4.3)$$

the wave-front shape is determined to be

$$z(r) = \frac{r_2 - r_1}{\Delta f} r - \left(f_1 - \frac{r_1}{r_2 - r_1} \Delta f \right) \left(\frac{r_2 - r_1}{\Delta f} \right)^2 \ln \left[f_1 + \frac{\Delta f}{r_2 - r_1} (r - r_1) \right] \Bigg|_{r_1}^r. \quad (4.4)$$

The weak gradient assumption allows the determination of the index of refraction by the optical path argument

$$n(0)t = n(r)t + z(r) \Rightarrow n(r) = n(0) - \frac{z(r)}{t}, \quad (4.5)$$

where $n(0)$, the index of refraction at the center of the axicon, is known a priori.

With eq. (4.4) for $z(r)$ and simplifying, the index profile for this GRIN axicon is

$$n(r) = n_0 - \frac{r_2 - r_1}{t(\Delta f)^2} \times \left\{ (r - r_1) \Delta f - [(r_2 - r_1) f_1 - r_1 \Delta f] \ln \left[1 + \frac{r - r_1}{r_2 - r_1} \frac{\Delta f}{f_1} \right] \right\}, \quad (4.6)$$

where n_0 is equal to $n(0)$. Assuming no central obscuration, $r_1=0$, the index expression reduces to the form

$$n(r) = n_0 - \frac{r_2}{t(\Delta f)^2} \left(r \Delta f - r_2 f_1 \ln \left[1 + \frac{r}{r_2} \frac{\Delta f}{f_1} \right] \right). \quad (4.7)$$

One can confirm this index equation by inspecting two limiting cases: $\Delta f \rightarrow 0$, and $f_1 \rightarrow 0$ when $r_1=0$. In the first case, by use of L'Hospital's Rule, the design is reduced to that of a unifocal lens. As expected, the index equation reduces to the quadratic radial-gradient form for a lens with back focal length f_l (i.e., a Wood lens),

$$\lim_{\Delta f \rightarrow 0} n(r) = n_0 - \frac{r^2}{2t f_l}. \quad (4.8)$$

In the second case, again found by use of L'Hospital's Rule, the focus begins at the back surface. The index equation reduces to a linear form, as expected, by analogy to a conical axicon,

$$\lim_{f_1 \rightarrow 0} n(r, r_1 = 0) = n_o - \frac{r_2}{t\Delta f} r. \quad (4.9)$$

Insight into the role of the GRIN profile is gained by writing equation (4.7) in a series expansion,

$$n(r) = n_o - \frac{1}{2tf_1} r^2 + \frac{\Delta f}{3r_2 tf_1^2} r^3 - \frac{(\Delta f)^2}{4r_2^2 tf_1^3} r^4 + \dots. \quad (4.10)$$

The first term is the index of refraction at the center of the axicon. The second term describes the paraxial base power of the lens. This focusing power provides the offset of the focal region from the back surface. The remaining terms are factors of Δf and are sources of aberration. Similar to theory of using an aberrated-lens system,⁶ this aberration can be viewed as providing the linear focal shift.

4.3. Design and Manufacture of Gradient-Index Axicon

4.3.1. Index Profile Prediction

With this understanding of how to determine the desired index profile needed for a GRIN axicon, two samples were designed and fabricated. The glass material (described in the *GRIN Fabrication* section) used was well characterized, and 2-mm-radius rods were available. Design goals were chosen that would not require too large of an index gradient for a 2 mm semi-aperture rod. The parameters chosen were n_o

equaled 1.60917, t was 5 mm, r_1 was 0 mm, r_2 was 2 mm, f_1 was 20 mm, and Δf was 15 mm.

If the design goals are used as the variables in the index equation [Eq. (4.7)], the resultant axicon behavior does not provide exactly the desired performance because the thin-lens assumption is violated. A numerical ray-tracing program is used to compute the theoretical focal curve with the design goals as the index-equation variables. This is compared with the desired focal curve in Figure 4.2; it is found to be between 4 and 5.5% less than the desired focal curve for any semi-aperture height.

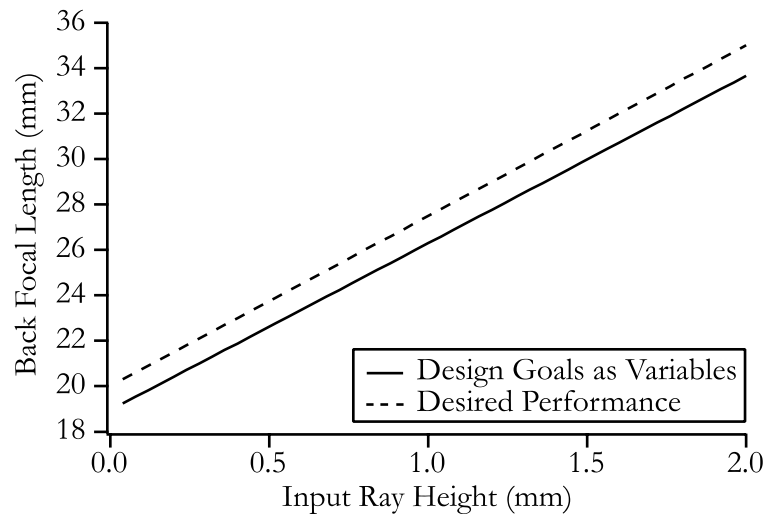


Figure 4.2. Simulated performance of axicon does not match desired, because design goals violate thin-lens assumption in index equation derivation. The difference in the back-focal lengths is not constant.

The index-equation variables must be adjusted to account for the sample thickness. To do so, a maximum-descent optimizer in the ray-trace program is used to determine modified f_1 and Δf values, \hat{f}_1 and $\hat{\Delta f}$. The optimized variables are functional variables for use in equation (4.7) to provide the index profile needed to

achieve the design goals; they should not be confused with the actual design goals. The optimized values are \hat{f}_1 is 21.06 mm, and $\Delta\hat{f}$ is 15.28 mm.

The index variables \hat{f} and $\Delta\hat{f}$ are larger than the design goal values f_1 and Δf by approximately 5 and 2%, respectively. The effect of the thin-lens assumption on the index of refraction for this case is shown in Figure 4.3. The thickness-corrected index is shallower than the index predicted with the design goals as index variables. This makes sense qualitatively and can be explained by use of an OPL argument. Because OPL is proportional to both the ray path length and the index of refraction, the index must decrease to maintain constant OPL as the ray path length increases. Since the thin-lens theory does not account for beam deviation and the actual ray paths in the lens are longer than predicted, the index of refraction decreases in total magnitude so that the desired OPL is achieved.

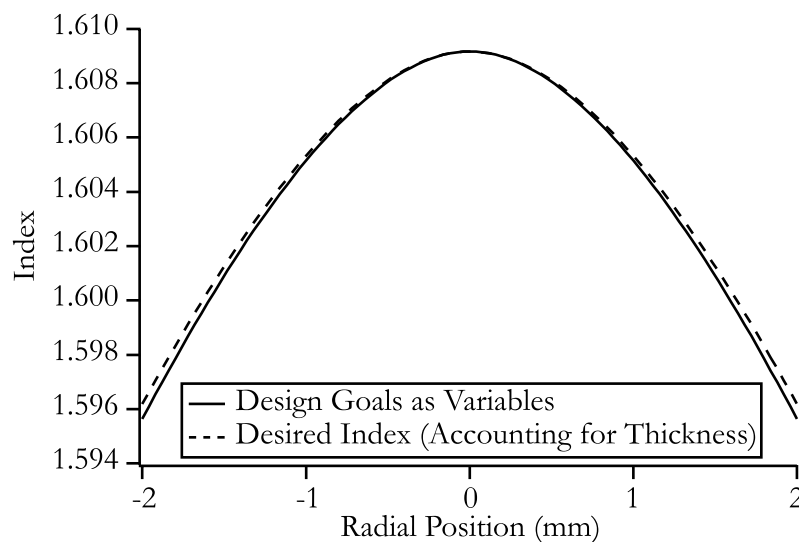


Figure 4.3. When sample thickness is accounted for, the necessary index of refraction has a slightly smaller index change than predicted by means of the thin-lens index equation.

4.3.2. Gradient-Index Fabrication

The necessary index of refraction profile for the design goals is now specified with equation (4.7) and the optimized variables given previously. However, the fabricated profile is determined by the ion-exchange process. One cannot compute ion-exchange parameters, such as diffusion time, temperature, and glass type from a desired refractive index function. However, a design-for-manufacture approach allows for the index profile calculation based on the ion-exchange process. One design-for-manufacture method for GRIN optics uses the modified quasi-chemical (MQC) diffusion model for the ion-exchange process.¹⁹ The expression for the MQC diffusion coefficient is given by

$$D(\chi) = \left[\frac{c}{2} \left(\frac{\chi\beta'(\chi=1) + (1-\chi)\beta'(\chi=0)}{\beta'} - 1 \right) + 1 \right] \frac{D_B}{1-\chi\alpha}, \quad (4.11)$$

$$\beta' = \sqrt{1 - 4(\chi - \chi_0)[1 - (\chi - \chi_0)](1 - \exp(\rho))},$$

where χ is the normalized sodium ion concentration and the fitting parameters are D_B , the self-diffusion coefficient; α , the mobility ratio; ρ , the interaction energy parameter; χ_0 , the peak position shift; and c , the coordination number. The MQC coefficients primarily depend on the glass composition and the ion-exchange temperature. The diffusion model is linked to optical design software to optimize the optical performance of the GRIN system with ion-exchange parameters as optimization variables.²⁰ Additional design parameters are obtained with TVBC diffusion, which

alternates between in-salt ion exchange and out-of-salt diffusion to control the final refractive index profile shape.²¹

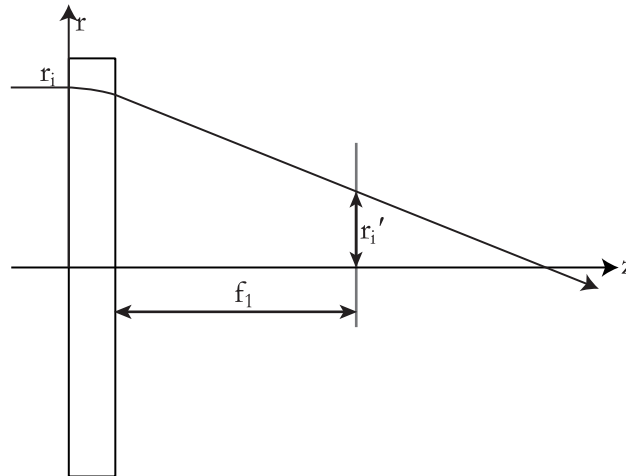


Figure 4.4. Parameters used to determine ray-intercept height at the start of the back focus for use in the optical design program's optimization process.

The TVBC diffusion design-for-manufacture model, which runs under OSLO Six as a dynamic-link library, is used to provide a manufacturable solution to the axicon design problem. To describe the axicon's desired performance, the desired ray-intercept heights are specified at a plane located at the start of the focal region, using the design goals. (See Figure 4.4) The ray height at f_1 for a given ray-input height is described by

$$r_i' = r_i - \frac{r_i}{f_1 + \Delta f \frac{r_i - r_1}{r_2 - r_1}} f_1. \quad (4.12)$$

These ray heights are used as target values or operands for the damped least-squares optimization in OSLO. The rays are chosen and weighted with the five-ring Gaussian-

Quadrature pupil sampling routine in OSLO. The MQC design index is identical to the desired index for the design goals.

The fabricated axicon devices were made by sodium-for-lithium ion exchange between custom-melted glass CHGL-25, which, per Harkrider's research²², had the following composition (in mole fraction),

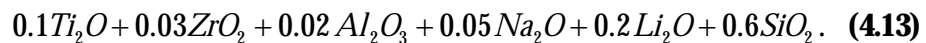


Table 4.1 shows the CHGL-25 MQC coefficients for ion exchange with molten sodium nitrate salt at 560 °C. Additionally, the conversion from normalized sodium concentration to refractive index is given by the following equation,

$$n(\chi) = 1.6234 - 0.03025\chi - 0.01098\chi^2. \quad (4.14)$$

The glass rod was prepared by core drill and centerless ground to 4.05 mm in diameter, the length is 49 mm, and the mass is 1.633 g. The ion exchange was performed in a top-loading furnace with 210 g of American Chemical Society-grade sodium nitrate in a stainless-steel beaker. The in-salt ion exchange time was 16.13 hours, after which the sample was cooled and ultrasonically cleaned with water. The out-of-salt diffusion step was performed in the same oven, which was ramped to 560 °C at 10 °C/min, held for 5.6 hours, and then cooled.²²

D_B	α	ρ	χ_0	c
0.095	0.23	-1.96	-0.06	9.6

Table 4.1. MQC coefficients for glass CHGL-25 at 560 °C. These parameters represent the diffusion coefficient in the TVBC diffusion design-for-manufacture model.

4.4. Experimental Testing and Results

4.4.1. Index Profile Measurement and Representation

The actual index profile of the diffused rod was determined to predict and to compare expected and actual performances of the final axicon samples. The radial index profile of the diffused rod was measured from a thin sample, at a wavelength of 632.8 nm, with an ac harmonic phase-shifting Mach-Zehnder interferometer. The measured index profile was close to the desired index in the center (See Figure 4.5).

The wings at the edges of the index were from chips in the sample edge.

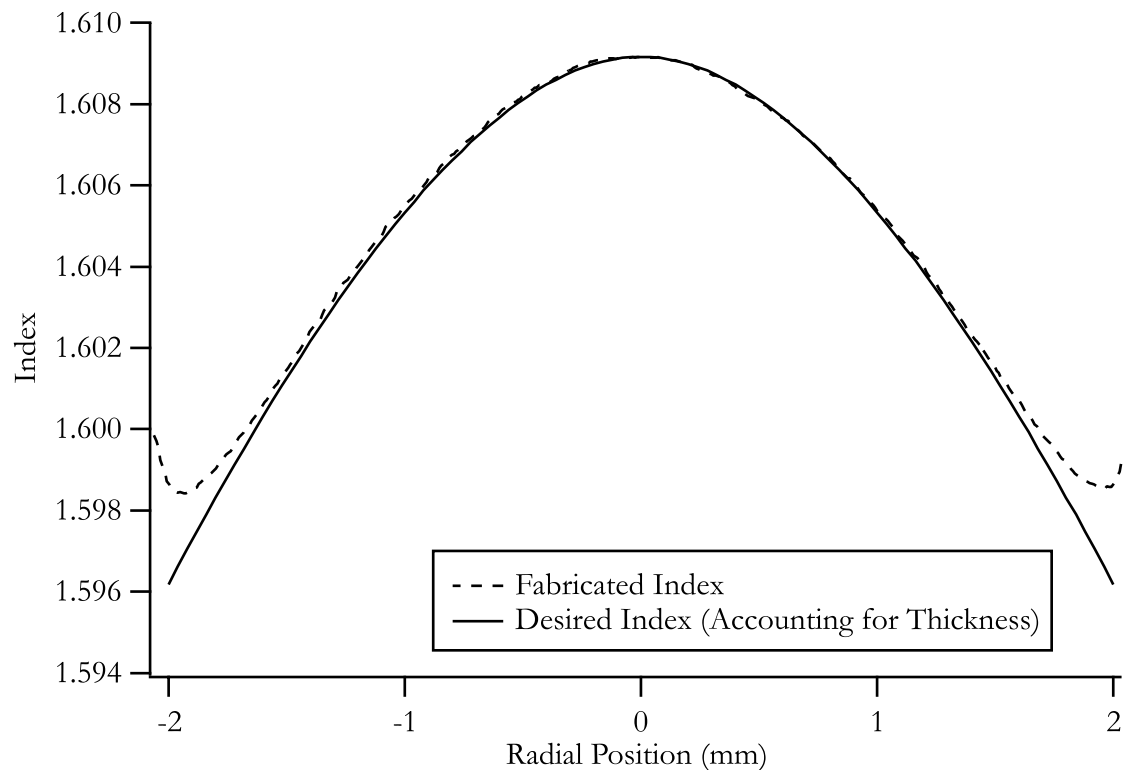


Figure 4.5. Measured index profile (from the fabricated sample) compared with the desired index profile. The wings at the edges of the measured data are from chips in the sample edges.

There was some concern about how best to represent the data. Typically in GRIN studies, the index data is fit with an even-order polynomial. That does not work very well for this particular case. To illustrate this, the desired index profile is represented with second, fourth, eighth, and sixteenth even-order polynomials and the theoretical axicon performance computed by means of ray-tracing using the fit results. Except for the constant power of the second-order fit, Figure 4.6 shows that the polynomial fit consistently causes an over-estimation of the near and the far focal lengths. The fit converges with increasing polynomial order, but it can only be accurately represented with a high-order polynomial; generally, this is not a good idea for fitting real data.

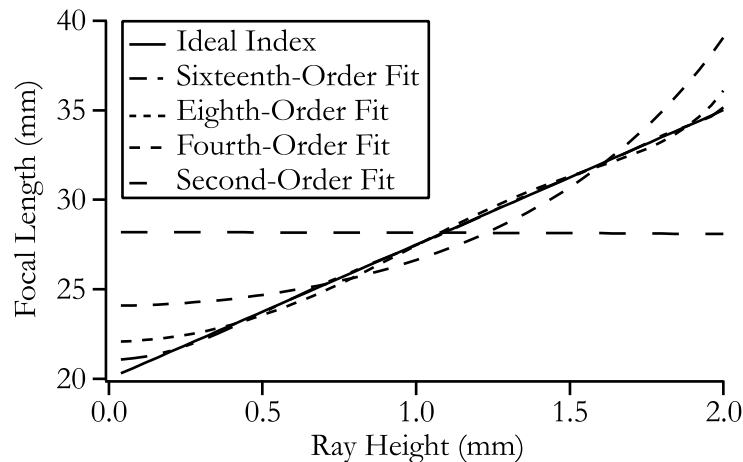


Figure 4.6. Theoretical performance of an ideal axicon compared with the polynomial approximation of an index. Even a higher- (sixteenth) order polynomial fails to predict the axicon's focal behavior accurately.

An alternative approach is to fit the data with the analytical index equation. In doing that, there is a risk of fitting to what is desired and not accounting for all the features in the actual index profile. However, since a polynomial does not fit the data accurately, this alternative is chosen.

Because the wings of the measured profile would adversely affect the quality of the fit, the edges of the index were not used in the fit. The region of the profile fit was determined by fitting various extents of the profile data and observing the resultant residual error. This region was determined to account for the maximum extent possible, while not incurring a significant increase in the residual error. The region fit was the central 1.65 mm of the total 2.0-mm radius. With the notation used in the section 4.3.1, the fitting variables were \hat{t} , \hat{r}_2 , \hat{f} , and $\Delta\hat{f}$; \hat{h}_0 and \hat{r}_1 were held constant at their original values. The results are shown in Figure 4.7 and in Table 4.2.

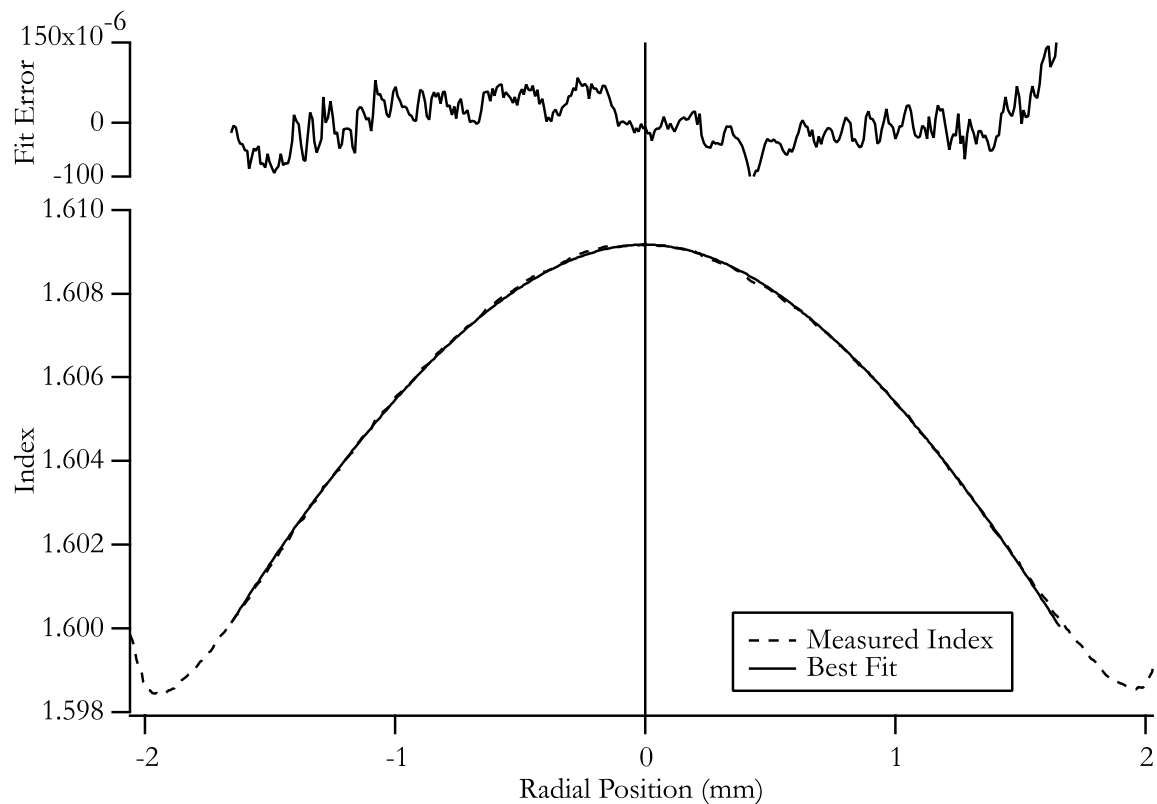


Figure 4.7. Analytical index formula was fit to the measured index profile over 1.65 mm of the 2.0-mm semi aperture.

$\hat{n}_o = 1.60917$	$\hat{t} = 5.029 \text{ mm}$
$\hat{r}_1 = 0 \text{ mm}$	$\hat{r}_2 = 1.870 \text{ mm}$
$\hat{f}_1 = 21.162 \text{ mm}$	$\Delta\hat{f} = 15.622 \text{ mm}$

Table 4.2. Index profile fit parameters.

4.4.2. Axicon Measurements

From the rest of the length is 49 mm diffused rod, two more segments were cut and polished, and were used to study the focal behavior of axicons made from this index profile. These two segments were made at the same time, and the their lengths and surface wedges measured. (See Table 4.3.) These wedges are polishing errors. They were determined by reflecting a laser beam from the surfaces and measuring its deviation from perfect retro-reflection.

Sample	Length (mm)	Wedge 1 (°)	Wedge 2 (°)
Axicon 1	7.04 ± 0.04	1.9 ± 0.1	4.9 ± 0.1
Axicon 2	3.51 ± 0.02	1.2 ± 0.1	1.9 ± 0.1

Table 4.3. Fabricated axicon dimensions.

The test apparatus (See Figure 4.8) was a spatially filtered and collimated He-Ne (632.8 nm) laser beam incident on the front face of an axicon sample, behind which was a microscope objective. A computer-controlled CCD camera captured the objective's image. The computer software allowed the image to be centered and transverse intensity profiles (horizontal in the image plane) to be acquired. The two axicon samples were tested individually.

As the imaging objective was scanned away from the sample, the initial focus was found to begin with a spot. With further distance, rings formed about the center

spot, soon showing a structure similar to a Bessel beam (and are shown to be pseudo-Bessel beams in the analysis). Four typical images are also shown in Figure 4.8.

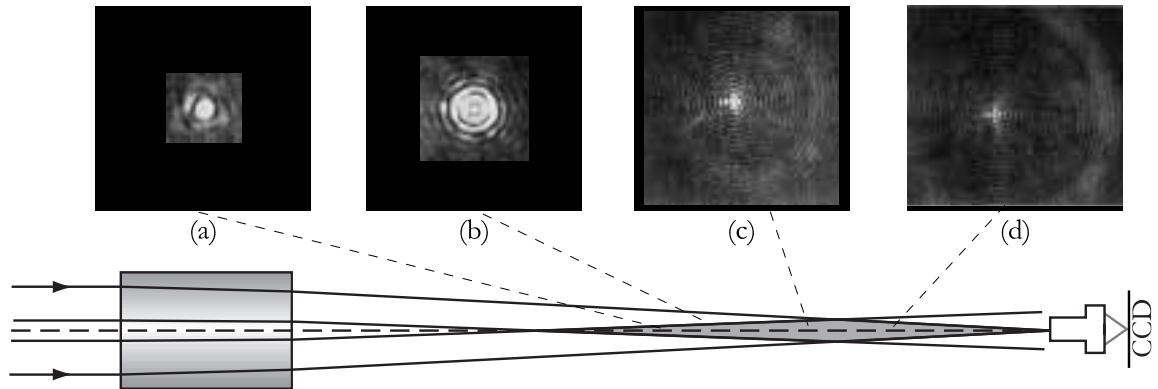


Figure 4.8. Experimental setup for measuring the axicon focus and example images from the axicon 2 beam. (a) Initial focus. (b) Appearance of first two full rings. (c) and (d) Images taken further along focus to show full pseudo-Bessel beam.

The objective was positioned to image what was considered the beginning of the focal region of the axicon. The initial focus was determined by the appearance of a well-defined circular spot. The transverse intensity profile was sampled, and the objective was translated 1000 μm . This process was repeated until the end of the focal region was reached. At the position where the central intensity was one-tenth its peak value, the rings were difficult to discern and difficult to distinguish from noise in the computer-acquired data. For this reason, the one-tenth peak position was chosen as the end-of-focus position. This was done for both samples. The intensity values were normalized relative to each measurement set.

Using the intensity data, two aspects of the axicons' behavior were examined: central-peak width and back focal length. From these analyses, it could be determined

if the samples produced the expected extended focus and whether they produced a pseudo-Bessel beam.

4.4.3. Axicon Analysis

The measured peak-intensity widths were compared with both theoretical predictions for this system and the widths predicted for a pseudo-Bessel beam. (See Figure 4.9 and Figure 4.10.) The theoretical peak-intensity widths of the axicons were computed by propagation of the coherent wave front at the back surface using the Fresnel diffraction approximation.²³ The axicons were modeled in Code V, and the wave front was numerically determined with that program. The wave front was then expressed as wave-front aberration relative to a spherical (converging) reference wave front of a desired radius. The propagation of the aberrated wave front to the plane of the reference sphere's focus was numerically computed using a fast Fourier transform method. Selection of the desired reference wave-front radius allowed the wave front to be propagated to any desired position. From the result, the peak width at that position was determined. Placement of the reference-sphere focus at various positions along the back focal length, permitted the peak width to be computed along the entire focal region.

The Fresnel propagation results showed good agreement with the measured data when the data of axicons 1 and 2 were shifted longitudinally by +0.5 and +0.75 mm, respectively. This suggested that the measured position of the samples is in error by those amounts. This showed that the measured peak widths have the expected size at the predicted position, showing that the axicons behaved as predicted.

It is also of interest whether the axicons produced pseudo-Bessel beams. As Herman and Wiggins¹⁸ explain, a pseudo-Bessel beam is expected for an axicon with a focal shift. Although not producing a true diffractionless beam, it behaves as such paraxially. Thus, for a perfect axicon with a focal offset, at any given focal position, the intensity profile is proportional to

$$J_0(kr \sin[\theta(z)])^2,$$

where $k = 2\pi / \lambda$ is the illumination wavenumber, r is an axis perpendicular to optical axis z , and θ is the slope at the back surface of the ray which crosses the optical axis at z . The difference between a true diffraction-free beam and a pseudo-diffractionless beam is easily seen in the behavior of the width of the central peak. It is constant over the entire focal region for a true diffraction-free beam, whereas it changes with distance along the optical axis for a Bessel like beam. The peak width is given by the first zero of the Bessel function

$$w_c = 2 \frac{2.408}{k \sin[\theta(z)]}. \quad (4.15)$$

The peak width was computed over the measured focal range for axicons 1 and 2. The axicons were modeled in Code V, and exact ray-trace simulations were run to calculate the geometrically predicted focal region and ray slope $\theta(z)$. The predicted ray slopes were used to compute the ideal peak widths with equation (4.15).

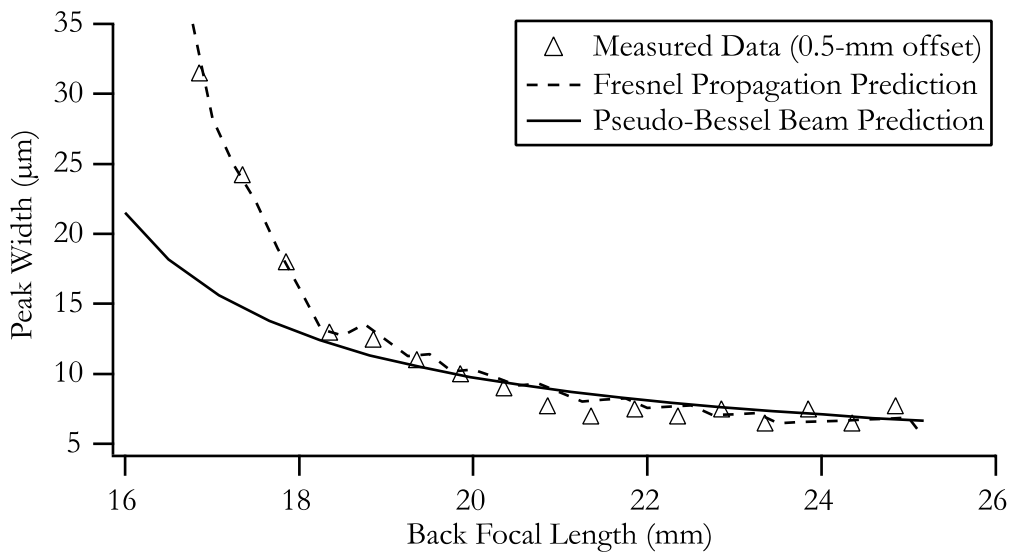


Figure 4.9. Measured peak widths for axicon 1 compared with prediction and pseudo-Bessel beam theory. Axicon 1 positions are shifted +0.5 mm for best agreement.

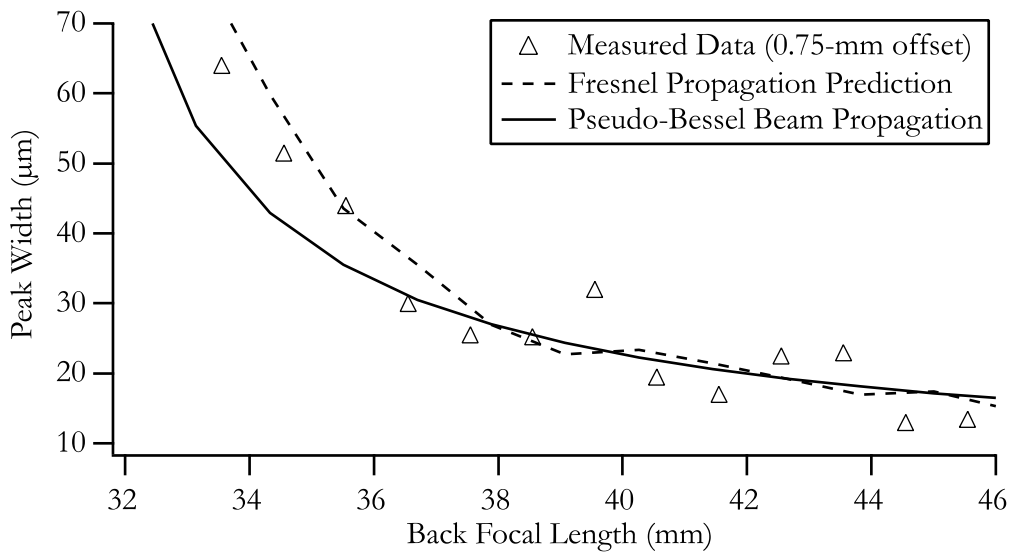


Figure 4.10. Measured peak widths for axicon 2 compared with prediction and pseudo-Bessel beam theory. Axicon 2 positions are shifted +0.75 mm for best agreement.

The analytical predictions for the pseudo-Bessel beam widths agree well with both the measured data and the numerical prediction in the latter extent of the focal

region, indicating that the axicons are producing a pseudo-Bessel beam. The longitudinally shifted data deviates from the prediction at the start of the focal region, suggesting that the ringed beam structure is not truly a diffractionless beam initially. It is also seen that axicon 2, with a longer starting focal position, has better agreement than axicon 1, with a shorter initial focus. This suggests that slower lenses, with the subsequent longer focal lengths, function more readily as pseudo-Bessel beam elements.

Geometric predictions for back focal lengths are computed with the index-fit results and measured axicon lengths, with the index-fit semi aperture of 1.65 mm. Rays are traced through the axicons over the semi aperture, and the minimum and the maximum back focal lengths are computed from the results. This provides estimations of the focal region, without accounting for diffraction effects. The measured and predicted focal lengths are summarized in Table 4.4. Although they do not seem to agree well, the disparities are understood in view of the peak-width calculations. For both axicons, the geometric focal lengths begin closer to the sample than was measured. But this initial focus prediction is the first position at which rays cross the optical axis, whereas the first measured starting point is at a distinct focus, which occurs farther along the optical axis. The predicted geometric end of focus for axicon 1 is closer than expected. The difference in values suggests that diffraction effects allow the focus to extend farther than can be accounted for by geometrical predictions. This is confirmed by the previous Fresnel propagation predictions, which show the beam extending to the measured distance. For axicon 2, the predicted end of focus is more distant than measured. This shows that the focus continues past the final measurement

position but is essentially unmeasurable because the intensity is too low. It is seen that because the geometric predictions do not account for diffraction effects, they do not give an exact prediction for the focal-length extent.

A few other points can be made from the measured focal lengths. The focal length scales almost linearly with length. Axicon 1 is twice as long as axicon 2, and its measured starting focal position is half the distance as for axicon 2. Likewise, the ending focal position is nearly half as distant. This shows that the axicon performance is almost linearly proportional to length.

Axicon	Measured (mm)			Geometrical Prediction (mm)		
	Start	End	Length	Start	End	Length
1	16.3 ± 0.1	24.3 ± 0.1	8.0 ± 0.1	13.612	23.147	9.535
2	32.8 ± 0.1	44.8 ± 0.1	12.0 ± 0.1	29.578	49.165	19.587

Table 4.4. Comparison of measured focal lengths to geometrical predictions with the index-fit results and the measured axicon lengths.

4.5. Conclusions

The fabricated axicons displayed extended foci. The widths of the central intensity peak had good agreement with theoretical predictions. Furthermore, the widths corresponded well with predictions for pseudo-Bessel beams in the latter portion of the focal region, which shows that these GRIN axicons produce both the line focus and the pseudo-diffractionless beam that is found for other axicons, such as aberrated-lens systems, conical axicons, and diffractive elements.

Thus, for the first time, a GRIN axicon has been designed, fabricated and tested. It is demonstrated that a GRIN element can produce a Bessel-like beam output,

with the subsequent extended focal region. Both the understanding of gradient-index design and axicon design are furthered.

Geometrical optics calculations, with a thin-lens approximation, are successfully used for the design and performance predictions. This greatly simplifies an otherwise challenging design process, based on wave propagation within gradient-index media. Also, the index profile has odd-power terms (in the series expansion). This is significantly different from conventional GRIN design, which uses only even-order polynomial series. This provides new insights, and uses, for odd-ordered polynomial forms of index profiles.

Finally, this illustrates the flexibility of the design methods described previously. Though nominally intended for ophthalmic lenses, they are equally effective in designing an axicon—a non-imaging system with wholly different performance goals.

4.6. References

- ¹John H. McLeod, “The Axicon: A New Type of Optical Element,” *Journal of the Optical Society of America* **44** (8), 592-597 (1954).
- ²John H. McLeod, “Axicons and Their Uses,” *Journal of the Optical Society of America* **50** (2), 166-169 (1960).
- ³J. Durnin, J. J. Miceli, Jr., and J. H. Eberly, “Diffraction-free beams,” *Physical Review Letters* **58** (15), 1499-501 (1987).
- ⁴D. DeBeer, S. R. Hartmann, R. Friedberg *et al.*, “Comment on 'Diffraction-free beams' (with reply),” *Physical Review Letters* **59** (22), 2611-12 (1987).

⁵Shiro Fujiwara, "Optical Properties of Conic Surfaces. I. Reflecting Cone," *Journal of the Optical Society of America* **52** (3), 287-92 (1962).

⁶Z. Jaroszewicz and T. Morales, "Lens axicons: systems composed of a diverging aberrated lens and a perfect converging lens," *Journal of the Optical Society of America A Optics & Image Science* **15** (9), 2383-90 (1998).

⁷J. Sochacki, A. Kolodziejczyk, Z. Jaroszewicz *et al.*, "Nonparaxial design of generalized axicons," *Applied Optics* **31** (25), 5326-30 (1992).

⁸J. P. Bowen, J. B. Caldwell, L. R. Gardner *et al.*, "Radial gradient-index eyepiece design," *Applied Optics* **27** (15), 3170-6 (1988).

⁹M. Deguchi, D. T. Moore, and D. S. Kindred, "Zoom lens design using gradient-index lenses," *SPIE Proceedings* **2173**, 161-8 (1994).

¹⁰D. S. Kindred and D. T. Moore, "Design, fabrication, and testing of a gradient-index binocular objective," *Applied Optics* **27** (3), 492-5 (1988).

¹¹J. L. Rouke, M. K. Crawford, D. J. Fischer *et al.*, "Design of three-element night-vision goggle objectives," *Applied Optics* **37** (4), 622-6 (1998).

¹²T. H. Tomkinson, J. L. Bentley, M. K. Crawford *et al.*, "Rigid endoscopic relay systems: a comparative study," *Applied Optics* **35** (34), 6674-83 (1996).

¹³E. W. Marchand, "Axicon gradient lenses," *Applied Optics* **29** (28), 4001-2 (1990).

¹⁴R. M. Gonzalez, J. Linares, and C. Gomez-Reino, "Gradient-index axicon lenses: a quasi-geometrical study," *Applied Optics* **33** (16), 3420-6 (1994).

- ¹⁵D. Huang, E. A. Swanson, C. P. Lin *et al.*, “Optical coherence tomography,” *Science* **254** (5035), 1178-81 (1991).
- ¹⁶S. D. Fantone, “Refractive index and spectral models for gradient-index materials,” *Applied Optics* **22** (3), 432-40 (1983).
- ¹⁷David J. Fischer, Curtis J. Harkrider, and Duncan T. Moore, “Design and manufacture of a gradient-index axicon,” *Applied Optics* **39** (16), 2687-2694 (2000).
- ¹⁸R. M. Herman and T. A. Wiggins, “Production and uses of diffractionless beams,” *Journal of the Optical Society of America A Optics & Image Science* **8** (6), 932-42 (1991).
- ¹⁹J. M. Inman, J. L. Bentley, and S. N. Houde-Walter, “Modeling ion-exchanged glass photonics: the modified quasi-chemical diffusion coefficient,” *Journal of Non Crystalline Solids* **191**, 1-2 (1995).
- ²⁰Julie Lynn Bentley, “Integration of the design and manufacture of gradient-index optical systems,” Ph. D., University of Rochester, 1995.
- ²¹C. J. Harkrider and D. T. Moore, “Time varying boundary condition diffusion for gradient-index design,” *SPIE Proceedings* **3482**, 780-8 (1998).
- ²²Curtis J. Harkrider, “Design-for-Manufacture of Gradient-Index Optical Systems using Time-Varying Boundary Condition Diffusion,” , University of Rochester, 1999.
- ²³Joseph W. Goodman, *Introduction to Fourier Optics* (McGraw-Hill, San Francisco, 1968).